

## Rotorcraft blade-vortex interaction noise prediction using the Lattice-Boltzmann method

Romani, Gianluca; Casalino, Damiano

**DOI**

[10.1016/j.ast.2019.03.029](https://doi.org/10.1016/j.ast.2019.03.029)

**Publication date**

2019

**Document Version**

Accepted author manuscript

**Published in**

Aerospace Science and Technology

**Citation (APA)**

Romani, G., & Casalino, D. (2019). Rotorcraft blade-vortex interaction noise prediction using the Lattice-Boltzmann method. *Aerospace Science and Technology*, *88*, 147-157.  
<https://doi.org/10.1016/j.ast.2019.03.029>

**Important note**

To cite this publication, please use the final published version (if applicable).  
Please check the document version above.

**Copyright**

Other than for strictly personal use, it is not permitted to download, forward or distribute the text or part of it, without the consent of the author(s) and/or copyright holder(s), unless the work is under an open content license such as Creative Commons.

**Takedown policy**

Please contact us and provide details if you believe this document breaches copyrights.  
We will remove access to the work immediately and investigate your claim.

# Rotorcraft Blade-Vortex Interaction Noise Prediction Using the Lattice-Boltzmann Method

Gianluca Romani<sup>1</sup>, Damiano Casalino<sup>2</sup>

*Delft University of Technology, 2629 HS, Delft, The Netherlands*

---

## Abstract

The aim of this paper is to assess the accuracy, capabilities and computational performances of the Lattice-Boltzmann/Very Large Eddy Simulation Method to predict the unsteady aerodynamic loads, the rotor wake development and the noise radiation of helicopter rotors in strong Blade-Vortex Interaction conditions. The numerical flow solution is obtained by solving the explicit, transient and compressible Lattice-Boltzmann equation implemented in the high-fidelity CFD/CAA solver Simulia PowerFLOW<sup>®</sup>. The acoustic far-field is computed by using the Ffwoes-Williams & Hawkings integral solution applied to a permeable surface encompassing the whole helicopter geometry. The employed benchmark configuration is the 40% geometrically and aeroelastically scaled model of a BO-105 4-bladed main rotor tested in the open-jet anechoic test section of the German-Dutch wind tunnel in the framework of the HART-II project. In the present study, only the baseline operating condition of the experimental campaign, without Higher-Harmonic Control enabled, is considered. All simulations are performed by assuming a rigid blade motion, but a computational strategy based on a combination of a rigid blade pitching motion and a transpiration velocity boundary condition applied on the blade surface is employed to take into account the blade elastic deformation motion measured during the experiments. As expected, modeling the blade elastic deformation leads to more accurate predictions of control settings, unsteady air-loads and noise footprint. The effects

---

<sup>1</sup>PhD Candidate, AWEP Department, [G.Romani@tudelft.nl](mailto:G.Romani@tudelft.nl)

<sup>2</sup>Professor of Aeracoustics, AWEP Department, [D.Casalino@tudelft.nl](mailto:D.Casalino@tudelft.nl)

of the computational grid on the aerodynamic and aeroacoustic prediction is documented as well.

*Keywords:* lattice-Boltzmann method, helicopters, blade-vortex interaction, aerodynamics, aeroacoustics

---

## 1. Introduction

This work describes an application of the Lattice-Boltzmann Method (LBM) solver Simulia PowerFLOW<sup>®</sup> to the evaluation of the aerodynamic and aeroacoustic fields around helicopter rotors in strong Blade-Vortex Interaction (BVI) conditions.

Helicopter BVI is a phenomenon which occurs when a rotor blade interacts very closely with tip vortices released by the other blades or the considered blade itself, and it typically occurs during descent flights or maneuvers at moderate advance ratio, when the wake of the main rotor remains in proximity of the rotor itself. The induced fluctuations of the blade aerodynamic loads represent one of the main sources of helicopter community noise and fuselage vibration. BVI noise is indeed considered as one of the major limitations of helicopter operation in urban areas, and it is strongly correlated with hundreds of dormant heliports worldwide.

The physics of BVI is governed by the structure and trajectory of the tip vortices, and in particular by the minimum distance from the rotor blade for the blade section and azimuth considered, which is referred to as blade-vortex miss distance [1]. For this reason, in order to successfully predict BVI phenomena, it is required to adopt an aerodynamic solver able to accurately predict three-dimensional unsteady flows and the spatial evolution of the wake vorticity, as well as to take into account the periodic elastic deformation of the rotor blades.

In the last two decades, many researchers have focused their efforts on experimental characterization and numerical prediction of BVI. In this framework, the second Higher-Harmonic Control (HHC) Aeroacoustic Rotor Test (HART-II) represents the best-known benchmark case for helicopter aerody-

namics, aeroelasticity and aeroacoustics [2, 3, 4, 5, 6]. The HART-II experiments were conducted in the large low-speed facility of the German-Dutch wind tunnel (DNW) in 2001 by an international cooperation between DLR, Onera, DNW, US Army AFDD and NASA Langley. The experimental database includes blade deflections, section air-loads, wake geometry, PIV and acoustic radiation measurements. Due to the large and comprehensive data sets available, this database is widely used by the rotorcraft research community for the validation of numerical solvers. In Refs. [7, 8] an assessment of the state-of-the-art of the comprehensive codes used within the HART II International Workshop is provided, whereas in Refs. [9, 10] a review of the state-of-the-art of Computational Fluid Dynamics methods coupled with Computational Structural Dynamics codes (CFD/CSD) is presented. Comprehensive codes are typically based on finite element beam formulations as structural model and two-dimensional blade-section theories, enhanced by corrections for unsteadiness and free-wake vortex lattice approaches, coupled with roll-up models (in order to identify the higher intensity vortex structures), to include the rotor wake influence on the aerodynamic loads. Among the plethora of comprehensive codes, those based upon the coupling of beam-like models for the blade structural dynamics and Boundary Element Methods (BEM) for its aerodynamics deserve a special mention due to their wide usage and good accuracy in predicting the aero-acousto-elastic behavior of helicopter rotors in BVI [11, 12]. The main advantage of comprehensive codes is the significantly lower CPU and memory requirements compared to CFD/CSD coupled approaches, making them suitable for fast trend parameters identification, optimization and mission-level analysis purposes. On the other hand, comprehensive codes typically requires to tune some of the parameters involved in their aerodynamic modules to obtain a good agreement between experimental data and numerical results [13], and they offer a lower potential in terms of accuracy with respect to that provided by CFD-based methods [8]. For both the aforementioned approaches, the noise radiation is typically evaluated using formulations based on the Ffowcs-Williams & Hawkings (FW-H) acoustic analogy equation [14] applied to the rotor aerodynamic

solution.

In recent years, LBM has been developed as an alternative CFD method for numerical simulations of unsteady turbulent flows. In contrast to Navier-  
60 Stokes equation-based methods, which describe the fluid at continuum level, LBM describes the fluid in terms of a discrete kinetic energy equation for particle density distributions and the macroscopic flow properties are direct result of the moments of these particle distribution functions [15, 16, 17]. The key advantages of LBM, compared to Navier-Stokes based methods, are the highly  
65 efficient parallelization (due to its explicit and local character), the ease of modeling various complex fluids, and the more straightforward handling of complex geometries and boundary conditions [16, 17, 18]. Moreover, due to the fact that LBM is low dissipative, compressible and provides an unsteady solution, it is intrinsically suited for aeroacoustic simulations. This has enabled LBM to be a  
70 very promising CFD method for large scale computations of complex industrial problems such as fixed-wing aircraft, both at component level [19, 20] and full aircraft level [21, 22], and turbofan aeroacoustics [23, 24].

The primary goal of this study is to assess the accuracy, capabilities and the computational performances of LBM to predict the unsteady air-loads, the  
75 rotor wake development and the noise radiation of rotors undergoing BVI conditions. Moreover, it is worth mentioning that the use of LBM to accomplish a rotorcraft aerodynamic and aeroacoustic benchmark study constitutes a further original contribution of the present paper. In this work, the HART-II baseline configuration, without Higher-Harmonic Control (HHC), is simulated by using  
80 the recently released version 5.4 of the LBM-based solver PowerFLOW<sup>®</sup> which implements a new LBM formulation that extends its applicability to transonic flow conditions [25]. The benchmark study is conducted by investigating the effects of mesh resolution first, and then by analyzing the impact of different blade deformation modelling assumptions on the accuracy of the aerodynamic  
85 and aeroacoustic results. The performances of the solver are reported for the sake of comparison with those of conventional CFD methods based on the discretization of Unsteady Reynolds Average Navier-Stokes (URANS) equations,

which are supposed, for this application, to generate an equivalent amount of flow information at an equivalent level of fidelity.

90 The paper is organized as follows. In Sec. 2, an overview of the underlying elements of the LBM-Very Large Eddy Simulation (VLES) are presented, along with the far-field noise prediction methodology and the computational strategy adopted to take into account the effects due to the elastic motion of the blades. In Sec. 3 the computational test case and setup are described. Section 4 is  
95 focused on the effects of the mesh resolution and blade deformation modelling on the accuracy of the numerical predictions. Finally, the main conclusions of this work are drawn in the fifth and conclusive section.

## 2. Numerical approach

In this section, the underlying elements of the LBM-VLES model imple-  
100 mented in PowerFLOW<sup>®</sup> are presented first. Then, the description of far-field noise radiation methodology is briefly outlined. Finally, the computational approach adopted to model the experimental blade elastic deformation is provided.

### 2.1. LBM-VLES flow solver

The LBM core of the CFD/CAA solver PowerFLOW<sup>®</sup> solves the Boltzmann  
105 equation for the distribution function  $f(\mathbf{x}, t, \mathbf{v})$  on a hexahedral mesh automatically generated around bodies, which consist of one or more connected solid parts. The function  $f$  represents the probability to find, in the elementary volume  $d\mathbf{x}$  around  $\mathbf{x}$  and in the infinitesimal time interval  $(t, t + dt)$ , a number of fluid particles with velocity in the interval  $(\mathbf{v}, \mathbf{v} + d\mathbf{v})$ . The Boltzmann equation  
110 is solved by discretizing the space velocity domain into a prescribed number of values in magnitude and direction. These discrete velocity vectors are such that, in a prescribed time step, one particle can be advected from one point of the mesh to  $N$  neighbouring points, including the point itself. For transonic flow simulations, a number of 39 stencil points are used (D3Q39, namely 3 di-  
115 mensions, 39 velocity states). It can be demonstrated that using 39 particle

velocity states ensures sufficient lattice symmetry to recover the Navier-Stokes equations for a non isothermal flow up to a Mach number of about 2 [25]. The standard LBM formulation is based on the (dimensionless) time-explicit advection equation:

$$f_i(\mathbf{x} + \mathbf{v}_i \Delta t, t + \Delta t) - f_i(\mathbf{x}, t) = C_i(\mathbf{x}, t), \quad (1)$$

120 where  $f_i$  represents the particle distribution function along the  $i$ -th direction, according to the finite set of discrete velocities ( $\mathbf{v}_i$ :  $i = 0, \dots, 38$ ), and  $\mathbf{v}_i \Delta t$  and  $\Delta t$  are the space and time increments, respectively. The left-hand side of Eq. 1 corresponds to the particle advection, while the right-hand side is the collision operator, which represents the rate of change of  $f_i$  resulting from  
125 collision (i.e. the interaction of particles). The collision term  $C_i$  is modelled with the well-known Bhatnagar-Gross-Krook (BGK) approximation [15, 26]:

$$C_i(\mathbf{x}, t) = -\Delta t / \tau [f_i(\mathbf{x}, t) - f_i^{eq}(\mathbf{x}, t)], \quad (2)$$

where  $\tau$  is the relaxation time parameter, which is related to the fluid dimensionless kinematic viscosity  $\nu$  and temperature  $T$  according to  $\tau = \nu / T + \Delta t / 2$ , and  $f_i^{eq}$  is the equilibrium distribution function, which is related to local hydrodynamic properties (density  $\rho$ , velocity  $\mathbf{u}$  and temperature  $T$ ) and is approximated by a fifth-order Hermite polynomial [25]:

$$\begin{aligned} f_i^{eq} = \rho \omega_i \bigg\{ & 1 + \mathbf{v}_i \mathbf{u} + \frac{1}{2} [(\mathbf{v}_i \mathbf{u})^2 - |\mathbf{u}|^2] + \frac{T-1}{2} (|\mathbf{v}_i|^2 - D) \\ & + \frac{\mathbf{v}_i \mathbf{u}}{6} [(\mathbf{v}_i \mathbf{u})^2 - 3|\mathbf{u}|^2] + \frac{T-1}{2} (\mathbf{v}_i \mathbf{u}) (|\mathbf{v}_i|^2 - D - 2) \\ & + \frac{1}{24} [(\mathbf{v}_i \mathbf{u})^4 - 6(\mathbf{v}_i \mathbf{u})^2 |\mathbf{u}|^2 + 3|\mathbf{u}|^2] \\ & + \frac{T-1}{4} [(|\mathbf{v}_i|^2 - D - 2)((\mathbf{v}_i \mathbf{u})^2 - |\mathbf{u}|^2) - 2(\mathbf{v}_i \mathbf{u})^2] \\ & + \frac{(T-1)^2}{28} [|\mathbf{v}_i|^4 - 2(D+2)|\mathbf{v}_i|^2 + D(D+2)] \\ & + \frac{\mathbf{v}_i \mathbf{u}}{120} [(\mathbf{v}_i \mathbf{u})^4 - 10(\mathbf{v}_i \mathbf{u})^2 |\mathbf{u}|^2 + 15|\mathbf{u}|^4] \\ & + \frac{T-1}{12} \mathbf{v}_i \mathbf{u} [(|\mathbf{v}_i|^2 - D - 4)((\mathbf{v}_i \mathbf{u})^2 - 3|\mathbf{u}|^2) - 2(\mathbf{v}_i \mathbf{u})^2] \\ & + \frac{(T-1)^2}{8} \mathbf{v}_i \mathbf{u} [|\mathbf{v}_i|^4 - 2(D+4)|\mathbf{v}_i|^2 + (D+2)(D+4)] \bigg\}, \quad (3) \end{aligned}$$

where  $D = 3$  denotes the spatial dimension and  $\omega_i$  are weighting parameters. For compressible flows, the LBM is coupled with an entropy partial differential equation to satisfy the conservation of energy (non isothermal model) [25]. Once the distribution function is computed, hydrodynamic flow quantities, such as flow density, velocity and temperature, can be determined through discrete integration of the distribution function  $f_i$ , i.e.  $\rho(\mathbf{x}, t) = \sum_i f_i(\mathbf{x}, t)$ ,  $\rho \mathbf{u}(\mathbf{x}, t) = \sum_i f_i(\mathbf{x}, t) \mathbf{v}_i$  and  $\rho e = \frac{D}{2} T = \sum_i f_i(\mathbf{x}, t) |\mathbf{v}_i - \mathbf{u}|^2$  (with  $e$  the internal energy), respectively. All the other physical quantities can be determined through thermodynamic relationships for an ideal gas.

Solving the lattice-Boltzmann equation is equivalent to performing a Direct Numerical Simulation (DNS) of the Navier-Stokes equations in the limits of the dynamic range (Mach number) that can be accurately covered by the number of discrete particle velocity vectors, and in the limits of the lattice resolution required to capture the smallest scales of turbulence. For high Reynolds flows, turbulence modelling is introduced [17] into the LBM scheme by solving a variant of the renormalization group (RNG)  $k - \epsilon$  model [27, 28] on the unresolved scales [29], selected via a swirl model [30]. This approach is referred to as LBM Very Large Eddy Simulation (LBM-VLES). More specifically, the two-equations based  $k - \epsilon$  RNG model is used to compute a turbulent relaxation time that is added to the viscous  $\tau$  relaxation time, i.e.  $\tau_{eff} \rightarrow \tau$ , where:

$$\tau_{eff} = \tau + C_\mu \frac{k^2/\epsilon}{(1 + \tilde{\eta}^2)^{1/2}}, \quad (4)$$

where  $C_\mu = 0.09$ ,  $k$  and  $\epsilon$  are the turbulent kinetic energy and dissipation, respectively, and  $\tilde{\eta}$  is a function of the local strain parameter  $\eta_s = k|\mathbf{S}|/\epsilon$ , local vorticity  $\eta_\omega = k|\boldsymbol{\Omega}|/\epsilon$  parameter and local helicity  $\eta_h = k(|\mathbf{u} \cdot \boldsymbol{\Omega}|/|\mathbf{u}|)/\epsilon$  parameter.

Because resolving the wall boundary layer by using a Cartesian mesh approach down to the viscous sub-layer in high Reynolds number applications is prohibitively expensive, a wall function approach is used in PowerFLOW<sup>®</sup> to model boundary layers on solid surfaces. The wall function model is an extension of the standard law-of-the-wall formulation [31] to include the effects of

favorable and adverse pressure gradients [29]:

$$u^+ = \frac{1}{\kappa} \ln\left(\frac{y^+}{A}\right) + B, \quad (5)$$

where  $u^+ = u/u_\tau$  and  $y^+ = yu_\tau/\nu$  are the well-known dimensionless velocity and wall-distance coordinate (with  $u_\tau = \sqrt{\tau_w/\rho}$  and  $\tau_w$  is the wall shear-stress), respectively,  $\kappa = 0.41$  and  $B = 5.0$  are empirically determined constants, and  
 160 A is a function of the pressure gradient. Such model takes into account the physical consequence that the velocity profile slows down and thus expands, due to the presence of an adverse pressure gradient, at least in the early stage of the development. The expression of the scaling function  $A$  is given by:

$$A = 1 + \delta \left| \frac{dp}{ds} \right| / \tau_w \quad \text{if } \hat{\mathbf{u}}_s \cdot \frac{dp}{ds} > 0 \quad (6)$$

$$A = 1 \quad \text{otherwise,} \quad (7)$$

where  $dp/ds$  is the stream-wise pressure gradient,  $\hat{\mathbf{u}}_s$  is the unit vector of the  
 165 local slip velocity and  $\delta$  is a length-scale equal to the size of the unresolved near-wall region. Eq. 5 is iteratively solved from the first cell close to the wall in order to specify the wall-shear stress for the wall boundary condition in the LBM scheme.

The LBM scheme is solved on a grid composed of cubic volumetric elements  
 170 (Voxels), the lattice, which is automatically created by the code. Different Variable Resolution (VR) regions can be defined by the user within the fluid domain in order to increase the volume discretization in regions of interest or where high flow gradients are expected. Being a Cartesian mesh used by the solver, a variable grid resolution by a factor of two is allowed between two adjacent VRs.  
 175 Moreover, since the solver uses an explicit time-marching scheme based on a unitary Courant-Friedrichs-Lewy condition (i.e.  $CFL = |\max(\mathbf{v}_i)\Delta t|/\Delta x = 1$ ), the time step is also varied (and automatically defined by the code according to the voxel size of a certain VR region  $\Delta x$  and the discrete particle velocities  $\mathbf{v}_i$ ) by a factor of two between two adjacent VRs. Therefore, the solution  
 180 in coarser VRs is updated at a lower rate compared to finer VRs, and a balanced domain decomposition based on the equivalent number of voxels updated

at every time step (i.e. Fine Equivalent Voxels, FEVoxels) allows a tremendous speed-up of the transient flow simulation. The surface of solid bodies is automatically facetized within each voxel intersecting the wall geometry using  
185 planar surface elements (Surfels). For the no-slip and slip wall boundary conditions at each of these elements, a boundary scheme [16] is implemented, based on a particle bounce-back process and a specular reflection process, respectively. Therefore, very complex arbitrary geometries can be treated automatically by the LBM solver, simplifying the tedious manual work typically associated with  
190 the volume meshing step using other CFD approaches.

### *2.2. Noise computations*

The CAA properties of LBM allows to analyze the acoustic near-field directly extracted from the transient flow solution. Due to the fact that the LBM is compressible and provides an unsteady solution, along with its low dissipation and  
195 dispersion properties [32], it is intrinsically suited for aeroacoustic simulations and allows to extract the sound pressure field directly in the near-field. In this work, both direct noise computations and FW-H far-field computations are performed. The employed FW-H solver [33] is based on a forward-time solution [34] of Farassat's formulation 1A [35] extended to a permeable (porous) integration  
200 surface encompassing the whole helicopter model. The necessity to accurately capture the near-field noise propagation from the source region up to the FW-H integration surface is a requirement that can take advantage of the intrinsic lower dissipation and low-dispersion properties of the LBM scheme compared to partial differential equation discretization schemes. The FW-H code used in  
205 this work is part of Simulia's post-processing software PowerACOUSTICS<sup>®</sup> 4.1, which is also used to perform statistical and spectral analysis of any unsteady solution generated by PowerFLOW<sup>®</sup>.

### *2.3. Blade deformation model*

The main affecting parameter of BVI phenomenon is the blade-vortex miss  
210 distance, which results from the instantaneous position of the convected tip

vortices and the deformed blades. Moreover, BVI mechanisms are strongly related to the azimuths of the interactions. Hence, in order to successfully predict BVI-related phenomena, it is crucial to fulfill the following three aspects: (i) the accurate prediction of the vortex trajectory, which mainly depends on the good rotor wake convection; (ii) the capability of the solver to convect vorticity with low dissipation and dispersion, thus preserving the vortex coherence over a sufficient number of rotor revolutions; (iii) the accurate prediction of the instantaneous position of the different blade sections, which relies on the capability of the solver to model elastic blade deformations under inertial and aerodynamic loads. Therefore, two-way-coupled high-fidelity CFD/CSD models represent the ultimate frontier of BVI noise prediction. As a primary step along a methodology maturation path, the present work is focused on the aerodynamic model only, and the flapping and torsional deformations are prescribed as measured in the HART-II experiments by means of Stereoscopic Pattern Recognition (SPR) technique [36, 37, 38]. More precisely, since the measurements were conducted using a coarse resolution, both in the azimuthal and radial directions, and since several measurement points were missing, an analytical reconstruction of the elastic blade motion is used in this work, which was performed by projecting Fourier components of the measured deformation on a basis of low-order FEM-computed modal shapes. Following van der Wall [39], the flap, lead-lag and torsion deformations for each blade can be respectively written as:

$$z(r, \Psi) = \sum_{i=1}^3 q_{z_i}(\Psi) \phi_{z_i}(r) \quad (8)$$

$$y(r, \Psi) = \sum_{i=1}^2 q_{y_i}(\Psi) \phi_{y_i}(r) \quad (9)$$

$$\phi(r, \Psi) = \sum_{i=1}^2 q_{x_i}(\Psi) \phi_{x_i}(r), \quad (10)$$

where  $\phi_{z_i}$ ,  $\phi_{y_i}$ ,  $\phi_{x_i}$  are the modal shapes, functions of the radial coordinate  $r$ :

$$\phi_{z_i}(r) = \sum_{j=0}^7 c_{z_{ij}} \left( \frac{r/R - 0.075}{1 - 0.075} \right)^j \quad (11)$$

$$\phi_{y_i}(r) = \sum_{j=0}^7 c_{y_{ij}} \left( \frac{r/R - 0.075}{1 - 0.075} \right)^j \quad (12)$$

$$\phi_{x_i}(r) = \sum_{j=0}^7 c_{x_{ij}} \left( \frac{r/R - 0.075}{1 - 0.075} \right)^j, \quad (13)$$

with  $R$  rotor radius, and  $q_{z_i}$ ,  $q_{y_i}$ ,  $q_{x_i}$  are the generalized coordinates:

$$q_{z_i}(\Psi) = \sum_{k=0}^6 (a_{z_{ik}} \cos(k\Psi) + b_{z_{ik}} \sin(k\Psi)) \quad (14)$$

$$q_{y_i}(\Psi) = \sum_{k=0}^6 (a_{y_{ik}} \cos(k\Psi) + b_{y_{ik}} \sin(k\Psi)) \quad (15)$$

$$q_{x_i}(\Psi) = \sum_{k=0}^6 (a_{x_{ik}} \cos(k\Psi) + b_{x_{ik}} \sin(k\Psi)), \quad (16)$$

which reproduce the periodic time dependency and magnitude of each elastic  
 235 deformation component through the azimuthal angle  $\Psi = \Omega t$ , with  $\Omega$  denoting  
 the rotational speed of the rotor. All the previous coefficients are available in  
 van der Wall's report [39]. Specifically, the coefficients of the mode shapes (Eqs.  
 11-13) are identical for each blade, whereas those of the generalized coordinates  
 (Eqs. 14-16) slightly differ for the four blades due to their non identical elastic  
 240 deformations. In this study, the coefficients in Eqs. 14-16 have been averaged  
 among the four blades in order to prescribe the same (mean) elastic deformation  
 time-histories to each blade. For the sake of completeness and to help the further  
 discussion of the numerical results, Fig. 1 depicts the analytical reconstruction of  
 the blade flap, lead-lag and torsion deflection data, averaged over the four blades,  
 245 as function of the radial coordinate and the azimuthal angle. As illustrated in  
 Fig. 1(a), the flap motion mainly shows a 1/rev content, with a relatively large  
 downward motion in the advancing side ( $0 - 180^\circ$ ) and a less pronounced upward  
 motion in the retreating side ( $180 - 360^\circ$ ). The lead-lag deflection also shows  
 a 1/rev variation with a maximum lag motion around  $180^\circ$  in the azimuth

250 (Fig. 1(b)). Finally, the torsional response (Fig. 1(c)) is predominantly 2/rev and negative, thus being responsible of an overall reduction of blade section angles of attack.

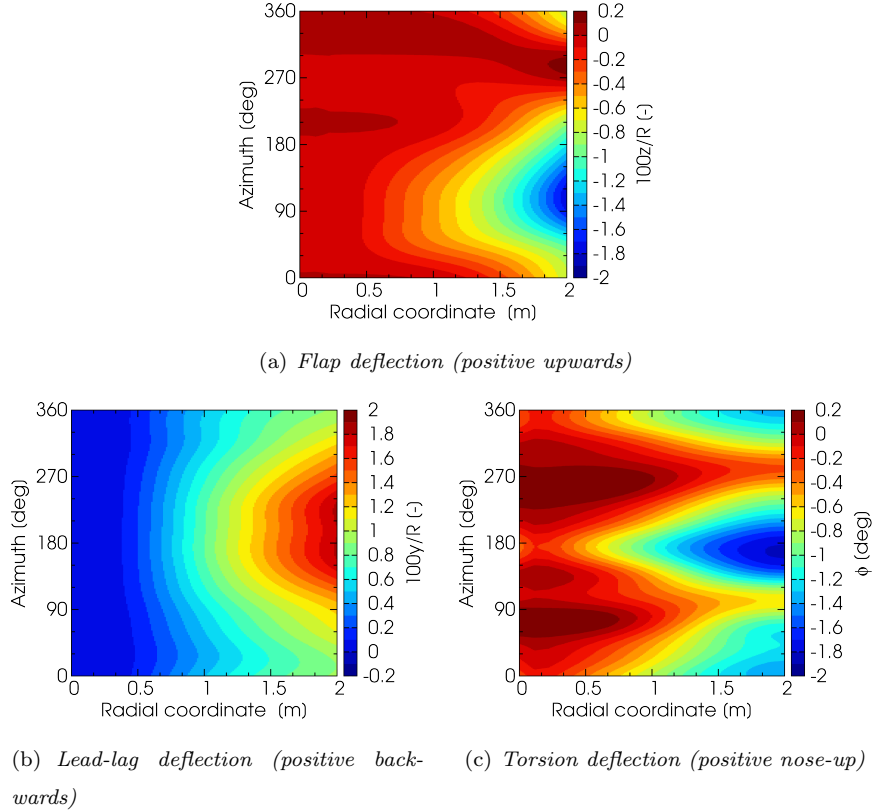


Figure 1: Analytical reconstruction of the HART-II baseline blade deflection data.

In this work, the blade elastic deformation is modelled by prescribing a combination of rigid motion and transpiration velocity boundary condition on the surface of the blades. This approach follows from the idea that a small-amplitude motion of the blade around its mean position can be modelled by applying a transpiration velocity boundary condition that has an equivalent dynamic effect on the blade. This approximation is imposed by the main limitation of the solver, which can simulate a combination of rigid rotations, but not a time-dependent deformation of the geometry. The computational mesh

is in fact generated automatically by the solver in a pre-processing stage and it is used throughout the simulation. The rigid rotation of parts respect to others is managed by creating partitions of the volume mesh in relative rotation called Local Reference Frames (LRFs) [40]. More specifically, in this work, the experimental blade flapping deformation (averaged over the four blades) is modelled by prescribing a transpiration velocity boundary condition equal to the time-derivative of Eq. 8 along the direction normal to the blade chord. The measured torsional deformation (averaged over the four blades) is instead modelled by prescribing a combination of a rigid blade pitching motion, equal to the experimental torsion at the 70% of the blade span, and a transpiration velocity boundary condition for the residual torsional component, namely the total torsion minus the one at the 70% of blade span. The first torsional contribution, say:

$$\phi(r = 0.7R, \Psi) = \sum_{i=1}^2 q_{x_i}(\Psi) \phi_{x_i}(r = 0.7R), \quad (17)$$

is added to the rigid blade pithing command, whereas the second contribution is modelled by prescribing the residual part of the torsion  $\Delta\phi(r, \Psi) = \phi(r, \Psi) - \phi(r = 0.7R, \Psi)$  as a dynamically equivalent flapping motion  $\dot{z}^{eq}(r, \Psi)$  along the direction normal to the blade chord, say:

$$\dot{z}^{eq}(r, \Psi) = -kU(r, \Psi) \tan(\Delta\phi(r, \Psi)), \quad (18)$$

where  $k=0.7$  is a coefficient tuned through comparisons between the lift generated by periodically pitching and plunging two-dimensional airfoils at the unitary reduced frequency, and  $U(r, \Psi) = \Omega r + U_\infty \sin(\Psi)$  is the local blade section velocity (being  $U_\infty$  the free-stream velocity). Finally, the lead-lag deflection motion is not expected to affect the BVI phenomenon significantly and is therefore neglected in the present study.

### 3. Computational test-case and setup

All simulations performed in this work are based on the same rotor operating conditions, which is the HART-II baseline configuration without HHC,

corresponding to a descent flight in strong BVI conditions. The effective rotor shaft angle is  $\alpha_{eff} = \alpha_s + \Delta\alpha = 4.5^\circ$  (with  $\alpha_s = 5.3^\circ$  is the rotor shaft angle and is  $\Delta\alpha = -0.8^\circ$  the wind tunnel interference angle, respectively) and its radius is  $R = 2$  m. The advance ratio is  $\mu = U_\infty \cos(\alpha_s) / (\Omega R) = 0.15$ , where  $U_\infty = 32.9$  m/s is the free-stream velocity and  $\Omega = 109.12$  rad/sec is the rotational speed of the rotor. This angular velocity corresponds to an hover Mach number of 0.639 and a blade-passing frequency (BPF) of 69.47 Hz. The ambient temperature and pressure are 290.45 K and 100970 Pa, respectively. Starting from the experimental collective ( $\theta_0$ ), lateral ( $\theta_c$ ) and longitudinal cyclic ( $\theta_s$ ) blade pitch commands as initial guess, a Newton-Raphson iterative method is used to trim the main rotor to the experimental thrust,  $T = 3300$  N, and hub rolling and pitching moment,  $M_x = 20$  Nm and  $M_y = -20$  Nm, respectively. Note that,  $\theta_0$ ,  $\theta_c$  and  $\theta_s$  are such that the blade pitch angle (positive nose-up) with respect to the blade pre-twist is defined as:

$$\theta(\Psi) = \theta_0 + \theta_c \cos(\Psi) + \theta_s \sin(\Psi), \quad (19)$$

The following set of three equations, representing the steady main rotor hub loads equilibrium (thrust, and rolling and pitching moments only), is considered:

$$f_1 = T - \hat{T}(\hat{\theta}_0, \hat{\theta}_c, \hat{\theta}_s) = 0 \quad (20)$$

$$f_2 = M_x - \hat{M}_x(\hat{\theta}_0, \hat{\theta}_c, \hat{\theta}_s) = 0 \quad (21)$$

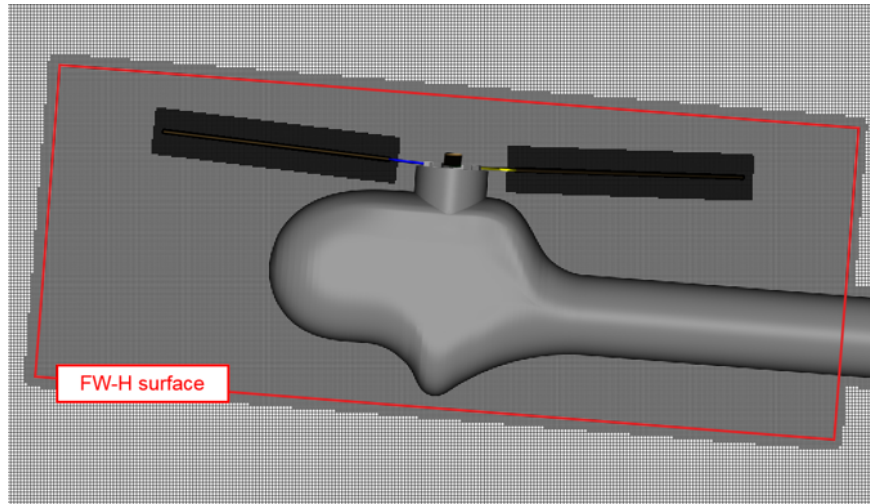
$$f_3 = M_y - \hat{M}_y(\hat{\theta}_0, \hat{\theta}_c, \hat{\theta}_s) = 0 \quad (22)$$

where  $\hat{T}$ ,  $\hat{M}_x$  and  $\hat{M}_y$  are the aerodynamic hub loads integrated over the main rotor blades, and  $\hat{\theta}_0$ ,  $\hat{\theta}_c$  and  $\hat{\theta}_s$  are the unknowns of the problem (i.e. the new trim settings). It should be noted that no inertial contributions appear in Eqs. 20-22 due to the steady flight condition considered in this study. As mentioned, the solution to the former set of equations is determined by using a Newton-Raphson scheme with a simplified Jacobian matrix, applying the following iterative procedure at the end of every main rotor revolution until convergence is reached (with  $n$  indicating the iteration step number):

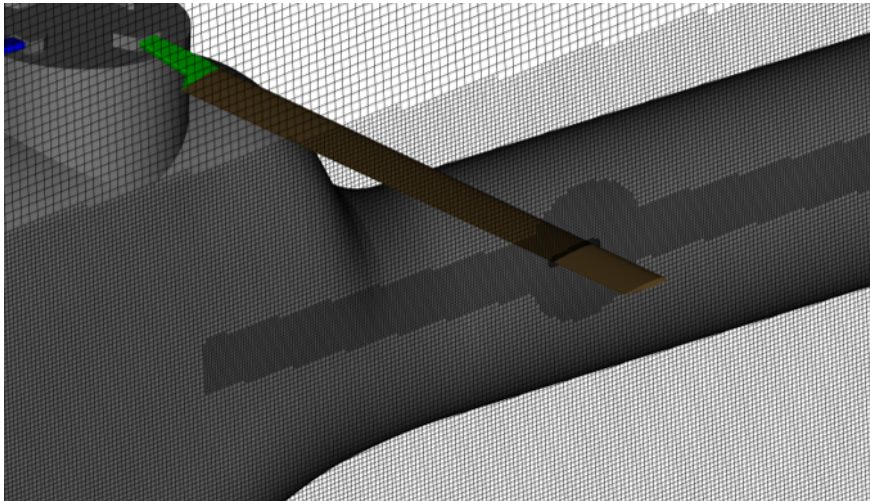
$$\Theta_n = \Theta_{n-1} - \mathbf{J}_0^{-1} \mathbf{f}_{n-1} \quad (23)$$

where  $\Theta_n = [\hat{\theta}_0, \hat{\theta}_c, \hat{\theta}_s]^T$ ,  $\mathbf{J}_0 = \partial(f_1, f_2, f_3)/\partial(\hat{\theta}_0, \hat{\theta}_c, \hat{\theta}_s)|_0$  is the Jacobian matrix evaluated at  $n = 0$  and  $\mathbf{f}_{n-1} = [f_1, f_2, f_3]^T_{n-1}$ . Note that, the approximation of  
 280 the fixed Jacobian matrix in Eq. 23 allows to evaluate the Jacobian matrix only one time, thus reducing the number of rotor revolutions required to obtain the problem solution (i.e. the trim condition).

A spherical simulation volume of radius  $100R$  centered around the helicopter is used. Static pressure and the free-stream velocity are prescribed on the outer  
 285 boundary, and an acoustic sponge approach is used to damp the out-going acoustic waves and thus minimize the backward reflection from the outer boundary. More specifically, the acoustic sponge is defined by two concentric spheres of radius  $10R$  and  $80R$ , respectively, and centered around the helicopter model. Hence, the fluid kinematic viscosity is gradually increased starting from its real  
 290 value within the inner sphere, up to an artificial value two orders of magnitude higher outside the outer one. Figures 2(a) and 2(b) show the computational grid used for all simulations presented in this section. Overall, 12 VR levels have been used to discretize the entire fluid domain. The finest VR level is set around the blades. The second finest VR is used to fill a blade tip annuls  
 295 and cylinders encompassing the blades, which are also used to define the blade pitching volumes. Throughout this paper, the noise radiation is computed by using a FW-H acoustic analogy applied to a permeable surface encompassing the whole helicopter model, as sketched in Fig. 2. Hence, the third finest VR level extends up to the FW-H permeable surface in order to ensure low acoustic  
 300 dissipation. Since the FW-H approach adopted in this study neglects the volume (quadrupole) term, spurious signals might arise when the permeable surface is intersected by vortical structures [41]. Therefore, in an early assessment stage of the computational setup, two strategies have been considered to assess the presence of such spurious signals: (i) removal of that portion of the  
 305 permeable FW-H surface intersected by the rotor wake, (ii) cap-averaging of the flow solution on staggered cups equipped on the permeable surface intersected by the rotor wake. It turned out that the two different approaches provided almost identical results, thus allowing the use of the whole FW-H permeable



(a) *Side view*



(b) *Close-up view*

Figure 2: Computational grid around the helicopter model, every second line shown for visualization purposes.

310 surface for far-field noise computations. Moreover, it should be pointed out as the above mentioned effects might also result negligible due to the fact that the scalar product between the local outward unit normal to the permeable surface and the unit radiation vector in the FW-H formulation [33] are close to zero,

or very small, for most of the microphones considered (as consequence of the relative position of that portion of the porous surface intersected by the vortical structures and the microphones), thus intrinsically damping out possible contaminations of the permeable surface. Acoustic data are sampled on the FW-H permeable surface at 68 kHz along 2 rotor revolutions (0.115 sec), after having reached the experimental trim conditions (10 rotor revolutions) for the thrust, and hub rolling and pitching moments. Fourier transforms of the near-field pressure are evaluated using a bandwidth of 35.3 Hz, 20% window overlap coefficient and Hanning weighting.

#### 4. Numerical results

In this section, a mesh resolution study is firstly conducted in order to establish a confidence level for the employed numerical setup. Then, the effects due to the incorporation of the blade elastic deformation in the numerical setup are investigated. The numerical results are compared to the experimental data from the HART-II test.

##### 4.1. Mesh resolution effects

As a sanity check of the quality of the computational mesh, a preliminary grid convergence study is conducted without modelling the blade elastic deformation (*fully-rigid* case). Three resolution levels are considered, hereinafter referred as *coarse*, *medium* and *fine*, corresponding to  $N = 42$ , 60 and 85 voxels per blade chord ( $c = 0.121$  m) in the finest VR, respectively ( $\sqrt{2}$  refinement ratio). The whole computational mesh is refined accordingly using the same VR scheme for all simulations. In order to highlight the effect of the mesh refinement only, the same collective and cyclic command angles are used for each resolution level, equal to those determined by applying the trim procedure on the finest computational grid. A summary of the grid size and the computational cost for the three refinement cases is reported in Tab. 1. Simulations are performed using a 1000 cores cluster with Intel Xeon CPU E5-2690 2.90 GHz and require, for the finest case, 3.2 hours per rotor revolution.

Table 1: Grid size in million of elements and computational cost.

Res. level	N	# Voxels	# FEVoxels	# Surfels	CPUh/rev
Coarse	42	113	25	5.4	849
Medium	60	249	60	6.7	1467
Fine	85	606	127	11.9	3168

#### 4.1.1. Rotor thrust

The mesh convergence is first examined in terms of trend of the Mean-Squared Relative Error (MSRE) between rotor thrust time-histories of two consecutive resolution levels:

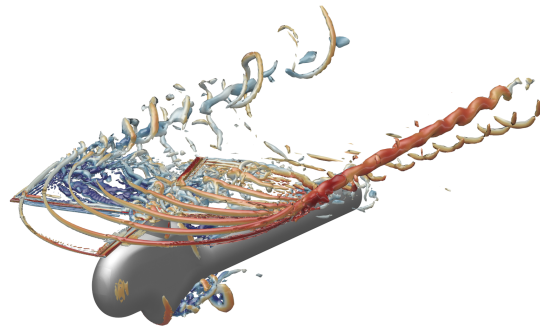
$$MSRE = \frac{1}{N_s} \sum_{i=1}^{N_s} \left( \frac{T_i^f - T_i^c}{T_i^f} \right)^2 \quad (24)$$

where  $N_s$  is the number of samples, whereas  $T_i^f$  and  $T_i^c$  are the rotor thrust samples of finest and coarsest of two consecutive resolution levels, respectively. Considering the steady statistically converged rotor thrust, the MSRE resulted in 0.0056 and 0.0016 for coarse-medium and medium-fine cases, respectively, thus revealing a convergence trend.

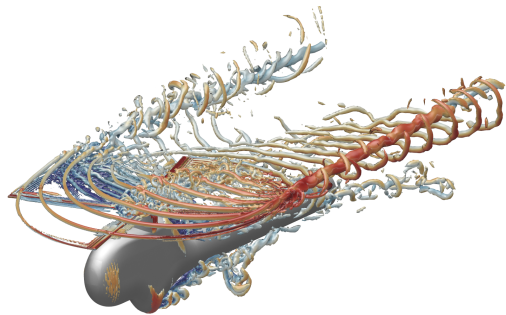
#### 4.1.2. Instantaneous vortical structures

Figures 3(a) to 3(c) show instantaneous snapshots of the blade tip vortex system for the three resolution levels extracted according to the  $\lambda_2$  criterion [42]. These images qualitatively illustrate that higher mesh resolutions result in lower diffusion of the vortical structures, which preserve their coherent character over a larger number of wake spirals. This aspect is crucial for an accurate BVI noise prediction generated by the interaction between one blade and the series of vortices from all blades. Interestingly, a multitude of turbulent scales can be observed, in particular downstream the hub wake, and in the advancing side of the rotor, where vortices breakdown occurs because of the higher relative velocities and strain rates. This is one of the advantages of a VLES turbulence modelling compared to URANS, and it is crucial to predict broadband noise

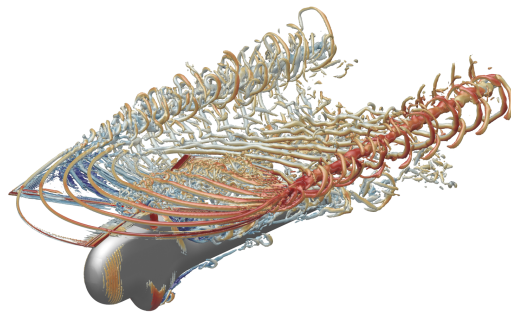
components. The presence of a larger amount of vortical structures for the fine case is in favor of their physical nature. A numerical instability origin, in fact,  
365 would have been enforced by a coarse resolution simulation.



(a) *Coarse resolution*



(b) *Medium resolution*



(c) *Fine resolution*

Figure 3:  $\lambda_2 = -7500 \text{ 1/s}^2$  iso-surfaces of the instantaneous flow around the helicopter model colored by velocity magnitude; mesh resolution effects.

#### 4.1.3. Unsteady air-loads

The sensitivity of the aerodynamic solution to the grid resolution is now evaluated in terms of unsteady air-loads. For each resolution level, Fig. 4 shows the  $c_n M^2$  coefficient time history (where  $c_n$  is the section normal force coefficient and  $M$  is the total local Mach number) at the span-wise section located at  $r/R=0.87$ . The  $c_n M^2$  exhibits a certain grid dependence, but a convergence trend can be observed regarding the azimuthal regions where BVI occurs. The discrepancies taking place roughly between  $90^\circ$  and  $270^\circ$ , among the three investigated resolution levels, could be ascribable to the different resolved suction pressure peak at the blade leading edge, as well as to the different up-wash velocity field induced by the front part of the helicopter fuselage, as consequence of the computational grid refinement. Concerning the azimuthal regions where BVI phenomenon occurs, the large spurious fluctuations occurring between  $60^\circ$  and  $90^\circ$  in the azimuth tend to decrease (and converge) as the mesh resolution is increased. Conversely, the fluctuations in the retreating side (i.e. between  $270^\circ$  and  $330^\circ$  in the azimuth) seem to be less affected by the mesh resolution.

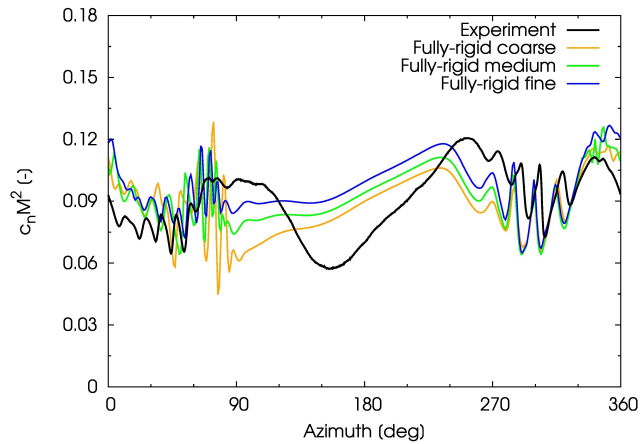


Figure 4: Time history of  $c_n M^2$  at  $r/R=0.87$ ; mesh resolution effects.

#### 4.1.4. Noise radiation

The mesh resolution analysis is concluded by examining the sensitivity of the noise radiation to the grid refinement. To this purpose, Fig. 5 shows the comparison between the experimental noise footprint on a horizontal plane located 2.2 m below the rotor hub and the numerical ones. Here, the noise contour maps are evaluated by integration of the FW-H equation on a porous surface encompassing the whole helicopter model. In order to highlight the BVI noise contribution, contour levels of the Overall Sound Pressure Level (OASPL) in the frequency range between the 6<sup>th</sup> and the 40<sup>th</sup> Blade Passage Frequency (BPF) are plotted. The improvement of the aerodynamic solution associated with the computational grid refinement, reflects directly into the improvement of the noise radiation prediction. Indeed, the noise footprint for the coarse mesh shows an overestimation of 6 dB of the high-noise region in the advancing side and an underestimation of 2 dB of the noise levels in the retreating side. Conversely, for the fine resolution case, the high-noise level lobe in the retreating side is correctly predicted, while the spot in the advancing side is overpredicted by 3-4 dB. From the above observations, it is possible to state that the fine mesh resolution provides satisfactory accuracy and convergence levels and can be used in the remainder of this work to illustrate the effects of the blade deformation modeling.

#### 4.2. Blade deformation effects

In this subsection, numerical results obtained by considering the fully-rigid rotor are compared to those obtained when the proposed elastic blade deformation approach is applied (*elastic* case). The comparison is carried out in terms of control settings, unsteady air-loads, vertical tip vortex positions and BVI noise footprint.

##### 4.2.1. Trim settings

Table 2 shows the comparison between the experimental collective ( $\theta_0$ ), lateral ( $\theta_c$ ), and longitudinal cyclic ( $\theta_s$ ), and those determined by applying the

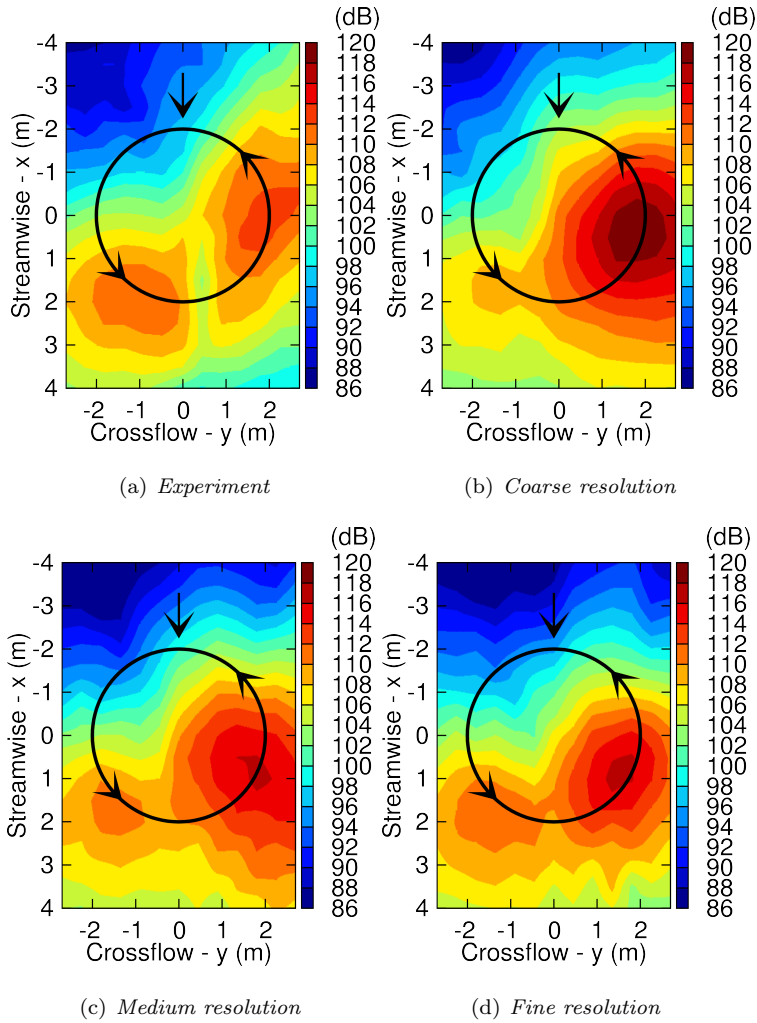


Figure 5: Effect of mesh resolution on BVI noise footprint; OASPL contour levels from FW-H results (6<sup>th</sup> to 40<sup>th</sup> BPF).

trim procedure to the fully-rigid and elastic case, respectively. Interestingly, the inclusion of elastic deformations leads to a substantial improvement of both the collective and cyclic commands prediction. This is a direct consequence of the more realistic incidence experienced by each blade section due to the sectional

415 angle of attack correction introduced by the blade deformation velocity acting on the surface of the blades.

Table 2: Blade deformation effects on control settings.

Case	$\theta_0$ [deg]	$\theta_c$ [deg]	$\theta_s$ [deg]
Experiment	3.80	1.92	-1.34
Fully-rigid fine	2.79	2.30	-1.87
Elastic fine	3.14	2.01	-1.55

#### 4.2.2. Unsteady air-loads

Figure 6 shows the effect of the blade elastic deformation modeling, as described in Section 2.2, on the  $c_n M^2$  at  $r/R = 0.87$ . Taking into account the blade elastic deformation results in a more accurate prediction of the sectional air-loads along most of the rotor revolution, especially on the retreating side for locations where strong blade-vortex interactions occur (i.e. between  $270^\circ$  and  $330^\circ$ ) and for the azimuthal sector between  $120^\circ$  and  $240^\circ$ , where the blade elastic torsion is mainly responsible for the low-frequency load variation (as depicted in Fig. 1(c)). This aspect is further quantitatively confirmed in terms of Pearson Correlation Coefficient (PCC) of the  $c_n M^2$  (which represents a measure of the linear correlation between experimental and numerical data), which turns out to be 0.3500 and 0.7876 for the fully-rigid and elastic cases, respectively.

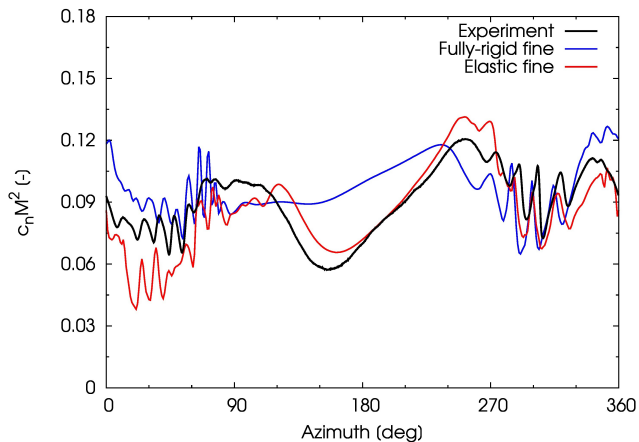
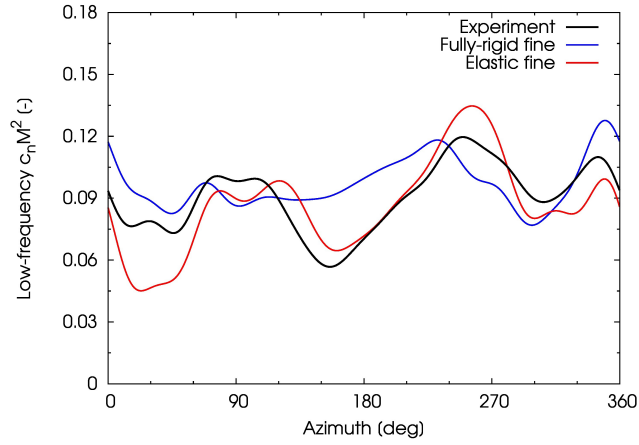


Figure 6: Time history of  $c_n M^2$  at  $r/R=0.87$ ; blade deformation effects.

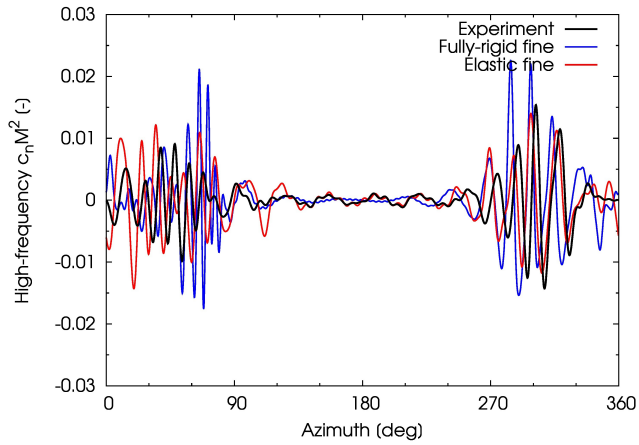
To better stress the aforementioned aspects, it is useful to decompose the  $c_n M^2$  coefficient into its low- and high-frequency contents. Indeed, it is worth mentioning that the low-frequency  $c_n M^2$  is mainly influenced by the rigid and elastic motion of the blade and thus gives a good indication on the quality of the employed elastic deformation model, whereas the high-frequency  $c_n M^2$  is mostly affected by BVI and hence can be used to examine the adequacy of the computational setup to predict BVI noise. The low-frequency contribution plotted in Fig. 7(a) confirms that the inclusion of the blade deformation improves the air-loads prediction, except for azimuthal position between  $0^\circ$  and  $60^\circ$ , where the low-frequency contribution of the elastic rotor case shows larger discrepancies compared to the fully-rigid rotor case. Moreover, as further highlighted in Fig. 7(b), taking into account the elastic blade deformation improves the accuracy of the high-frequency  $c_n M^2$  contribution as well, and thus BVI phenomenon detection. In particular, the amplitude and the azimuth of each fluctuation are better captured on the retreating side when the elastic approach is considered. Concerning the advancing side, both the fully-rigid and elastic computations are not in a very good agreement with the experiment. However, the elastic approach still shows an improvement for what concern the amplitude of the different blade-vortex interactions compared to the fully-rigid case.

#### 4.2.3. Tip-vortex trace

Figures 8(a) and 8(b) show the tip vortex position, in the hub reference frame, on two lateral planes placed in the advancing side ( $y\text{-hub} = 1.4$  m) and in the retreating side ( $y\text{-hub} = -1.4$  m), respectively. In this work, the tip vortex locations are determined by extracting the center of the vortex-core from vorticity magnitude contour plots. Following the vortex trajectory method applied to HART-II PIV data (Ref. [43]), advancing side traces for  $x\text{-hub} > 0$  m are identified when one of the rotor blades is at  $\Psi = 20^\circ$ , whereas those for  $x\text{-hub} < 0$  m correspond to  $\Psi = 70^\circ$ . Conversely, retreating side traces for  $x\text{-hub} > 0$  m and  $x\text{-hub} < 0$  m are extracted at  $\Psi = 70^\circ$  and  $\Psi = 20^\circ$ , respectively. Both in the advancing and retreating sides, modeling of the blade elastic



(a) Low-frequency  $c_n M^2$  content (up to 10/rev)

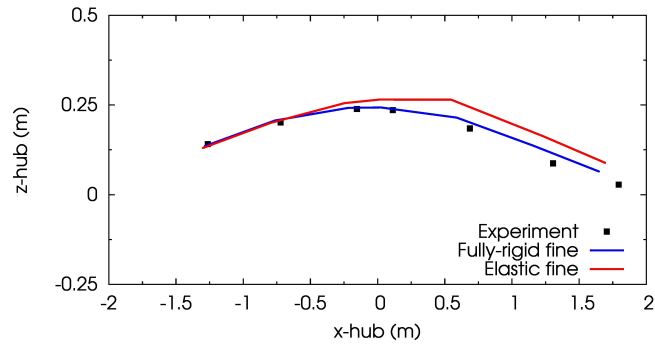


(b) High-frequency  $c_n M^2$  content (above 10/rev)

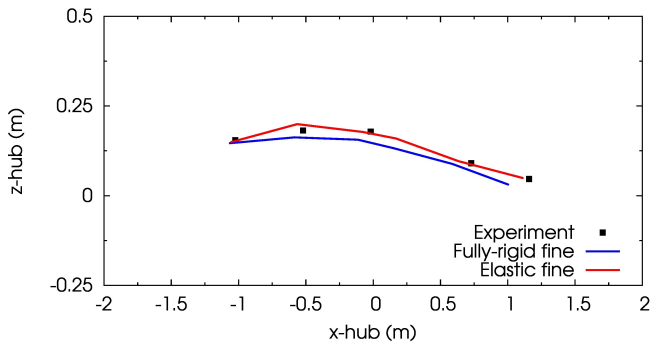
Figure 7: Frequency filtered  $c_n M^2$  time histories at  $r/R=0.87$ ; blade deformation effects.

deformations leads to a slightly higher wake position prediction with respect to  
 460 the fully-rigid case. In absolute terms, this is responsible of a partial worsening  
 of the wake shape prediction in the advancing side, downstream the rotor hub,  
 and of an overall improvement in the retreating side. As mentioned before, the  
 accurate prediction of the blade-vortex miss distance has a strong influence on  
 the pressure fluctuations induced by the tip vortices on the blade and, thus,

465 represents a crucial aspect in BVI noise prediction. In view of this, it is inter-  
 esting to point out that, for the elastic approach, the higher tip-vortex trace  
 on the advancing side leads to an earlier azimuthal occurrence of blade-vortex  
 interactions compared to experimental and fully-rigid results. Concerning the  
 retreating side, the better prediction of the wake shape directly reflects into the  
 470 better evaluation of unsteady air-loads, due to the fact that the experimental  
 flapping deflation is relatively small in the fourth quadrant of the rotor disk (i.e.  
 between  $270^\circ$  and  $360^\circ$  in the azimuth) as depicted in (Fig. 1(a)).



(a) *Advancing side, y-hub = 1.4 m*



(b) *Retreating side, y-hub = -1.4 m*

Figure 8: Tip-vortex trace on vertical planes; blade deformation effects.

#### 4.2.4. Noise radiation

To conclude the analysis on the blade deformation effects, Fig. 9 illustrates  
 475 the effects of the blade elastic deformation on the predicted BVI noise footprint

on a horizontal plane located 2.2 m below the rotor hub.

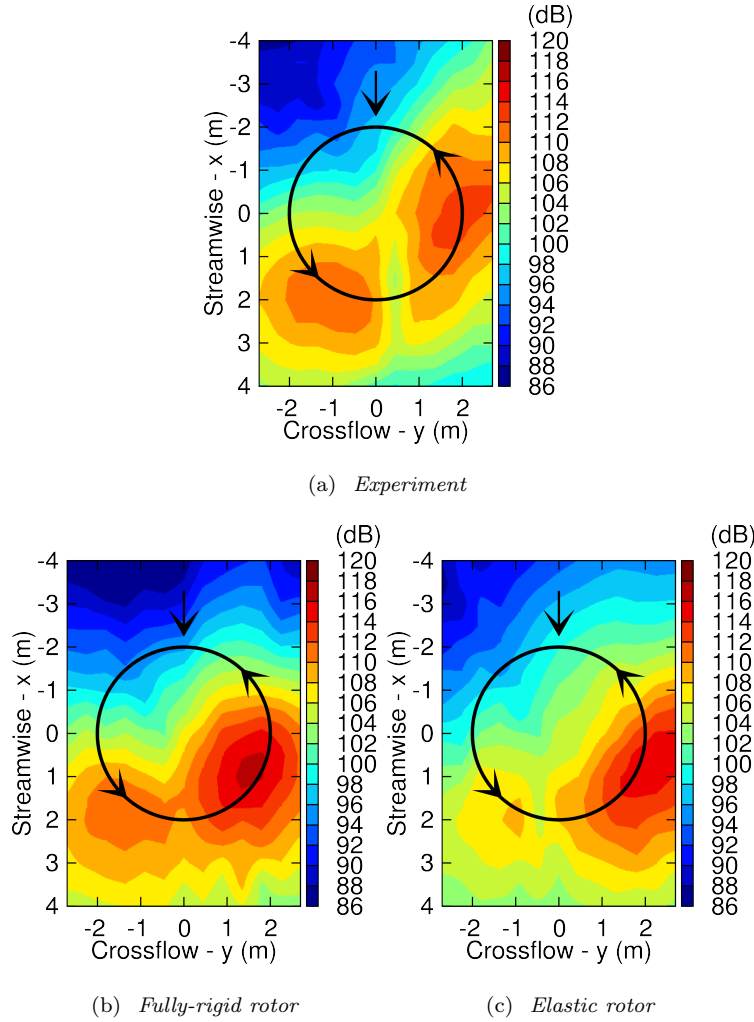


Figure 9: Effect of blade deformation on BVI noise footprint; OASPL contour levels from FW-H results (6<sup>th</sup> to 40<sup>th</sup> BPF).

As already stressed, modeling the elastic deformation improves the accuracy of BVI noise prediction, with a PCC of the OASPL footprint of 0.8794 for the fully-rigid case, and of 0.8873 for the elastic one. The elastic rotor setup is able to capture the overall noise directivity, as well as the high-noise lobe in the advancing side in a quite satisfactory way. Indeed, the noise levels in the

advancing side are slightly overpredicted by 1-2 dB, whereas the high-noise lobe in the retreating side is underestimated by 2-3 dB. Conversely, the rigid rotor results exhibit a better agreement with the measurements only in the retracting side, whereas the high-noise lobe in the advancing side is overestimated up to 4 dB, and the low-noise region in the top-left corner is not properly captured. However, it could be argued that the very good prediction of the retreating side high-noise lobe for the rigid case is merely the results of a certain level of acoustic dissipation occurring in the simulation and associated to the propagation of acoustic waves for a relatively long path in the simulation domain (i.e. from the rotor up to the FW-H permeable integration surface encompassing the whole helicopter model). Indeed, one would expect a better noise prediction in the retreating side for the elastic rotor case, due to the higher level of correlation with the experimental results of the high-frequency  $c_n M^2$ , compared to that of fully-rigid rotor case.

Finally, it is worth mentioning that the present level of accuracy for both fully-rigid and of elastic setups is overall higher than those obtained (at a lower computational cost) by using comprehensive codes, as reported in Refs. [7, 8], and quite satisfactory if compared to those obtained (at a comparable computational cost) by using either CFD with prescribed blade elastic motion [44] or CFD/CSD coupled approaches [13]. However, it should be recalled that, in contrast with the above mentioned comprehensive codes and CFD/CSD methods, the current elastic computation requires blade elastic deformations as inputs, in order to account for elasticity effects through the transpiration velocity boundary condition approach.

## 5. Conclusions

In this paper, the Lattice-Boltzmann/Very Large Eddy Simulation Method was applied for the first time to predict the unsteady air-loads, the rotor wake development and the noise radiation of helicopter rotors in BVI conditions. The considered benchmark was the baseline case of the HART-II experimen-

tal campaign. The numerical flow solution was obtained by solving the explicit, transient and compressible Lattice-Boltzmann equation implemented in the high-fidelity CFD/CAA solver Simulia PowerFLOW<sup>®</sup>. The acoustic far-field was computed by using the Ffwocs-Williams & Hawkings integral solution applied to a permeable surface encompassing the whole helicopter model. First, a mesh resolution study was conducted considering a fully-rigid rotor case and it revealed an acceptable level of mesh convergence, with reasonably good results in terms of noise footprint already obtained for a resolution of 60 voxels per blade chord at a CPU cost of 1467 hours per rotor revolution (medium resolution case). Then, a computational strategy based on a combination of a rigid blade pitching motion and a transpiration velocity boundary condition applied on the blade surface was employed to take into account the blade elastic deformation, leading to an improvement of control settings, sectional air-loads and noise radiation predictions compared to the fully-rigid rotor case. The level of accuracy of the present aeroacoustic results can be considered quite satisfactory if compared to that reported in the literature for comprehensive codes, CFD solvers with prescribed blade elastic motion and CFD/CSD coupled approaches. Although some intrinsic inaccuracies in the numerical results were observed, mainly due to the lack of the proper rotor blade elastic deformation modeling, the present study revealed the capability of the LBM to successfully simulate helicopter rotors in BVI conditions at engineering-level. The LBM may be therefore considered as an additional methodology for the prediction of helicopter BVI noise.

### **Acknowledgements**

The authors gratefully acknowledge the provision of data that was used in this study by the members of the HART II team.

## References

- [1] H. Y. Yung, Rotor Blade–Vortex Interaction Noise, *Progress in Aerospace Sciences* 36 (2) (2000) 97–115.
- 540 [2] Y. H. Yu, C. Tung, B. van der Wall, H.-J. Pausder, C. Burley, T. Brooks, P. Beaumier, Y. Delrieux, E. Mercker, K. Pengel, The HART-II test: Rotor Wakes and Aeroacoustics with Higher-Harmonic Pitch Control (hhc) Inputs-The Joint German/French/Dutch/Us Project, Tech. rep., DTIC Document (2002).
- 545 [3] B. G. van der Wall, B. Junker, C. Burley, T. Brooks, Y. Yu, C. Tung, M. Raffel, H. Richard, W. Wagner, E. Mercker, et al., The HART II Test in the LLF of the DNW-a Major Step Towards Rotor Wake Understanding, in: *Proceedings of the 28th European Rotorcraft Forum*, Bristol, England, 2002, pp. 273–284.
- 550 [4] J. W. Lim, C. Tung, Y. H. Yu, C. L. Burley, T. Brooks, D. Boyd, B. Van Der Wall, O. Schneider, H. Richard, M. Raffel, HART-II: Prediction of Blade-Vortex Interaction Loading, Tech. rep., DTIC Document (2003).
- [5] B. G. van der Wall, 2nd HHC Aeroacoustic Rotor Test (HART II)-Part I: Test Documentation, Institute Report, IB-111-2003/31, <ftp://HART-II@ftp.dlr.de>.
- 555
- [6] B. G. van der Wall, C. L. Burley, 2nd HHC Aeroacoustic Rotor Test (HART II)-Part II: Representative Results, Institute Report, IB-111-2005/34, <ftp://HART-II@ftp.dlr.de>.
- [7] B. G. van der Wall, J. W. Lim, M. J. Smith, S. N. Jung, J. Bailly, J. D. Baeder, D. D. J. Boyd, An Assessment of Comprehensive Code Prediction State-Of-The-Art Using the HART II International Workshop Data, AHS International 68th Annual Forum.
- 560

- [8] B. G. van der Wall, J. W. Lim, M. J. Smith, S. N. Jung, J. Bailly, J. D. Baeder, D. D. Boyd Jr, The HART II International Workshop: an Assessment of the State-of-the-art in Comprehensive Code Prediction, CEAS Aeronautical Journal 4 (3) (2013) 223–252.
- [9] M. J. Smith, J. W. Lim, B. G. van der Wall, J. D. Baeder, R. T. Biedron, D. D. Boyd Jr, B. Jayaraman, S. N. Jung, B.-Y. Min, An Assessment of CFD/CSD Prediction State-of-the-art Using the HART II International Workshop Data, in: 68th Annual Forum of the American Helicopter Society, Ft. Worth, TX, 2012.
- [10] M. J. Smith, J. W. Lim, B. G. van der Wall, J. D. Baeder, R. T. Biedron, D. D. Boyd Jr, B. Jayaraman, S. N. Jung, B.-Y. Min, The HART II International Workshop: an Assessment of the State of the Art in CFD/CSD Prediction, CEAS Aeronautical Journal 4 (4) (2013) 345–372.
- [11] G. Bernardini, J. Serafini, S. Lanniello, M. Gennaretti, Assessment of Computational Models for the Effect of Aeroelasticity on BVI Noise Prediction, International Journal of Aeroacoustics 6 (3) (2007) 199–222.
- [12] M. Gennaretti, G. Bernardini, J. Serafini, G. Romani, Rotorcraft Comprehensive Code Assessment for Blade–Vortex Interaction Conditions, Aerospace Science and Technology 80 (2018) 232–246.
- [13] D. D. Boyd Jr, HART-II Acoustic Predictions Using a Coupled CFD/CSD Method, AHS International 65th Annual Forum, Ft. Worth, TX.
- [14] J. E. Ffowcs Williams, D. L. Hawkins, Sound Generated by Turbulence and Surfaces in Arbitrary Motion, Philosophical Transactions of the Royal Society of London, Series A A264 (1151) (1969) 321–342.
- [15] H. Chen, S. Chen, W. Matthaeus, Recovery of the Navier-Stokes Equations Using a Lattice-Gas Boltzmann Method, Physical Review A 45 (8) (1992) 5339–5342.

- 590 [16] H. Chen, C. Teixeira, K. Molvig, Realization of Fluid Boundary Conditions  
via Discrete Boltzmann Dynamics, *International Journal of Modern Physics*  
C 9 (8) (1998) 1281–1292.
- [17] H. Chen, S. Kandasamy, S. A. Orszag, S. Succi, V. Yakhot, Extended Boltz-  
mann Kinetic Equation for Turbulent Flows, *Science* 301 (5633) (2003)  
595 633–636.
- [18] H. Chen, S. Orszag, I. Staroselsky, S. Succi, Expanded analogy between  
boltzmann kinetic theory of fluid and turbulence, *Journal of Fluid Me-  
chanics* 519 (2004) 301–314.
- [19] D. Casalino, A. F. P. Ribeiro, E. Fares, S. Nölting, Lattice-Boltzmann  
600 Aeroacoustic Analysis of the LAGOON Landing Gear Configuration, *AIAA*  
*Journal* 52 (6) (2014) 1232–1248.
- [20] D. Casalino, A. F. P. Ribeiro, E. Fares, Facing Rim Cavities Fluctuation  
Modes, *Journal of Sound and Vibration* 333 (13) (2014) 2812–2830.
- [21] M. R. Khorrami, E. Fares, D. Casalino, Towards Full Aircraft Airframe  
605 Noise Prediction: Lattice Boltzmann Simulations, *AIAA Paper* 2014-2481.
- [22] E. Fares, D. Casalino, M. Khorrami, Evaluation of Airframe Noise Reduc-  
tion Concepts via Simulations Using a Lattice Boltzmann Approach, *AIAA*  
*Paper* 2015-2988.
- [23] D. Casalino, A. Hazir, A. Mann, Turbofan Broadband Noise Prediction  
610 using the Lattice Boltzmann Method, *AIAA Paper* 2016-2945.
- [24] I. Gonzalez-Martino, D. Casalino, Fan Tonal and Broadband Noise Simu-  
lations at Transonic Operating Conditions Using Lattice-Boltzmann Meth-  
ods, in: *2018 AIAA/CEAS Aeroacoustics Conference*, 2018, p. 3919.
- [25] X. Nie, X. Shan, H. Chen, A Lattice-Boltzmann/Finite-Difference Hybrid  
615 Simulation of Transonic Flow, *AIAA Paper* 2009-0139.

- [26] P. L. Bhatnagar, E. P. Gross, M. Krook, A Model for Collision Processes in Gases. I. Small Amplitude Processes in Charged and Neutral One-Component Systems, *Physical Review* 94 (3) (1954) 511–525.
- [27] V. Yakhot, S. A. Orszag, Renormalization Group Analysis of Turbulence. I. Basic Theory, *Journal of Scientific Computing* 1 (1) (1986) 3–51.
- [28] V. Yakhot, S. A. Orszag, S. Thangam, T. B. Gatski, C. G. Speziale, Development of Turbulence Models for Shear Flows by a Double Expansion Technique, *Physics of Fluids A* 4 (7) (1992) 1510–1520.
- [29] C. M. Teixeira, Incorporating Turbulence Models into the Lattice-Boltzmann Method, *International Journal of Modern Physics C* 9 (1998) 1159–1175.
- [30] C. G. Alexander, H. Chen, S. Kandasamy, R. Shock, S. R. Govindappa, Simulations of Engineering Thermal Turbulent Flows Using a Lattice Boltzmann Based Algorithm, *ASME-PUBLICATIONS-PVP* 424 (2001) 115–126.
- [31] B. E. Launder, D. B. Spalding, The Numerical Computation of Turbulent Flows, *Computer Methods in Applied Mechanics and Engineering* 3 (1974) 269–269.
- [32] G. A. Brès, F. Pérot, D. M. Freed, Properties of the lattice-boltzmann method for acoustics, *AIAA Paper* 2009-3395.
- [33] G. A. Brès, F. Pérot, D. M. Freed, A Ffowcs Williams-Hawkings Solver for Lattice-Boltzmann Based Computational Aeroacoustics, *AIAA Paper* 2010-3711.
- [34] D. Casalino, An Advanced Time Approach for Acoustic Analogy Predictions, *Journal of Sound and Vibration* 261 (4) (2003) 583–612.
- [35] F. Farassat, G. P. Succi, The Prediction of Helicopter Discrete Frequency Noise, *Vertica* 7 (4) (1983) 309–320.

- [36] O. Schneider, B. G. van der Wall, Preparation of SPR Data from HART II, Institute Report, IB-111-2003/07, <ftp://HART-II@ftp.dlr.de>.
- 645 [37] O. Schneider, B. G. van der Wall, Preparation of SPR Data from HART II-Final Analyzing Methods and Results, Institute Report, IB-111-2003/20, <ftp://HART-II@ftp.dlr.de>.
- [38] O. Schneider, B. G. van der Wall, Completion of SPR Data Analysis from HART II, Institute Report, IB-111-2004/07, <ftp://HART-II@ftp.dlr.de>.
- 650 [39] B. G. van der Wall, Mode Identification and Data Synthesis of HART II Blade Deflection Data, Institute Report, IB-111-2007/28, <ftp://HART-II@ftp.dlr.de>.
- [40] R. Zhang, C. Sun, Y. Li, R. Satti, R. Shock, J. Hoch, H. Chen, Lattice Boltzmann Approach for Local Reference Frames, *Communications in*  
655 *Computational Physics* 9 (5) (2011) 1193–1205.
- [41] L. V. Lopes, D. D. Boyd Jr, D. M. Nark, K. E. Wiedemann, Identification of Spurious Signals from Permeable Ffowcs Williams and Hawkings Surfaces.
- [42] J. Jeong, F. Hussain, On the Identification of a Vortex, *Journal of Fluid Mechanics* 285 (1995) 69–94.
- 660 [43] F. Hoffmann, B. G. van der Wall, The Vortex Trajectory Method Applied to HART II PIV Data, Institute Report, IB-111-2005/34, <ftp://HART-II@ftp.dlr.de>.
- [44] G. Gopalan, J. Sitaraman, J. D. Baeder, F. H. Schmitz, Aerodynamic and Aeroacoustic Prediction Methodologies with Application to the HART II  
665 Model Rotor, AHS International 62nd Annual Forum, Phoenix, AZ.